



Self supervised contrastive learning for digital histopathology

Ozan Ciga ^{a,*}, Tony Xu ^{b,1}, Anne Louise Martel ^{a,c,2}



^a Department of Medical Biophysics, University of Toronto, Canada

^b Department of Electrical and Computer Engineering, University of British Columbia, Canada

^c Physical Sciences, Sunnybrook Research Institute, Toronto, Canada

ARTICLE INFO

Keywords:

Self supervised learning
Digital histopathology
Whole slide images
Unsupervised learning

ABSTRACT

Unsupervised learning has been a long-standing goal of machine learning and is especially important for medical image analysis, where the learning can compensate for the scarcity of labeled datasets. A promising subclass of unsupervised learning is self-supervised learning, which aims to learn salient features using the raw input as the learning signal. In this work, we tackle the issue of learning domain-specific features without any supervision to improve multiple task performances that are of interest to the digital histopathology community. We apply a contrastive self-supervised learning method to digital histopathology by collecting and pretraining on 57 histopathology datasets without any labels. We find that combining multiple multi-organ datasets with different types of staining and resolution properties improves the quality of the learned features. Furthermore, we find using more images for pretraining leads to a better performance in multiple downstream tasks, albeit there are diminishing returns as more unlabeled images are incorporated into the pretraining. Linear classifiers trained on top of the learned features show that networks pretrained on digital histopathology datasets perform better than ImageNet pretrained networks, boosting task performances by more than 28% in F_1 scores on average. Interestingly, we did not observe a consistent correlation between the pretraining dataset site or the organ versus the downstream task (e.g., pretraining with only breast images does not necessarily lead to a superior downstream task performance for breast-related tasks). These findings may also be useful when applying newer contrastive techniques to histopathology data. Pretrained PyTorch models are made publicly available at <https://github.com/ozanciga/self-supervised-histopathology>.

1. Introduction

The number of labeled images in machine learning tasks is found to be positively correlated with the task performance; however, labeled data is scarce and expensive. The problem is exacerbated in medical image analysis tasks, where expert annotations are often required and crowdsourcing is not usually an option. In many cases, labeling must also be done on-site due to regulations regarding dissemination of private patient data. In any medical image analysis task, the most laborious and time-consuming step tends to be labeling the data and several approaches have been proposed to mitigate this *data annotation bottleneck*. Unsupervised and self-supervised methods that can utilize unlabeled data, and semi-supervised methods that use partially labeled data, have been found to improve task performance (Campanella et al., 2019a; Komura & Ishikawa, 2018; Peikari, Salama, Nofech-Mozes, & Martel, 2018).

Until recently, most self-supervised techniques have relied on natural-scene image properties which are not applicable to histopathology images. However, recent contrastive learning approaches can be

applied to digital pathology images (see Section 2). In this work, we use residual networks pretrained with self-supervised learning to learn generalizable features. We employ SimCLR (Chen, Kornblith, Norouzi, & Hinton, 2020), a contrastive self-supervised technique that has comparable performance to the supervised ResNet 50 network on top-1 classification accuracy for the ILSVRC2012 dataset. We pretrain residual networks with this method and use the pretrained networks in downstream tasks for multiple tasks on multiple, multi-organ digital histopathology datasets. We explore different data sampling strategies to understand the amount and the type of data that leads to a representation that improves task performances over ImageNet pretraining or training from scratch. Specifically, we examine the impact of the number of images used for pretraining, resolution, staining, and tissue type on the learned representations and downstream task performance. Furthermore, we compare multiple image augmentation strategies to identify the best practices when pretraining for digital histopathology. Our results indicate that pretraining with unlabeled histopathology images can improve task performances over Imagenet pretraining and

* Correspondence to: Sunnybrook Health Sciences Centre, 2075 Bayview Ave., M6 609, Toronto, ON M4N 3M5, Canada.

E-mail addresses: ozan.ciga@mail.utoronto.ca (O. Ciga), tony.xu@alumni.ubc.ca (T. Xu), a.martel@utoronto.ca (A.L. Martel).

¹ Present address: Department of Electrical and Computer Engineering, University of British Columbia: 5500-2332 Main Mall, Vancouver, BC Canada V6T 1Z4.

² Present address: Sunnybrook Health Sciences Centre, 2075 Bayview Ave., M6 609, Toronto, ON M4N 3M5, Canada.

mitigate labeled data requirements for various classification, regression, and segmentation tasks.

2. Related work

Unsupervised learning has been a long-standing goal of computer-aided diagnostic systems. Previously, sparse and variational autoencoders have been used for unsupervised nuclei detection and transfer learning (e.g., learning filter banks at multiple scales) (Chang, Han, Zhong, Snijders, & Mao, 2017; Hou et al., 2019; Xu et al., 2015) and generative adversarial networks have been used for tissue and cell-level classification, nuclei segmentation, and cell counting (Hu et al., 2018). Most of these unsupervised methods are not applicable to structures larger than cells or to tasks more complicated than distinguishing tissue and cell types, mostly due to the small image sizes they are capable of working with (e.g., 64×64 pixels), and due to the limited information that can be encoded by such methods. They may also require custom networks, and may only be applicable to applications with specific resolution and staining properties.

Self-supervised learning is a promising subclass of unsupervised learning, where the raw input data is used to generate the learning signal instead of a prior such as mutual information or cluster density. These methods can generally be applied to larger images and work with standard architectures such as residual networks (He, Zhang, Ren, & Sun, 2016). Context-based self-supervised methods rearrange the image input and task the network to perform spatial reordering. For instance, Noroozi and Favaro (2016) tile an image into nine square pieces and then shuffle the tiles, whereas Gidaris, Singh, and Komodakis (2018) rotate the input image in 90° angles. In either case, the aim is to obtain the original input using a neural network, which is effectively pretrained for downstream tasks by performing predictions on tile orderings or rotation angles, respectively. While contextual information can be exploited in natural scene images to obtain meaningful representations, structures within histopathological images are elastic and may form infinitely many valid groupings. Therefore, these techniques are not directly applicable to the histology domain. For instance, predicting rotations is not a viable task for whole slide images, since cells and surrounding structures will have a valid arrangement in the rotated image as well. In histopathology, Gildenblat and Klaiman (2019) use spatial adjacency as a signal for similarity, and the pretraining task is to label image pairs as similar or dissimilar based on the spatial distance on a whole slide image. Tellez, Litjens, van der Laak, and Ciompi (2019) also utilize contrastive learning by applying augmentations on image patches extracted from WSIs. Their aim is to learn salient features by distinguishing if two augmented images are from the same source image.

More recently, contrastive approaches based on learning latent-space features by discriminating between unlabeled training samples achieved state-of-the-art results in computer vision tasks. Such contrastive learning methods assume that under minor transformations, two views of the same image patch should have similar feature representations (Becker & Hinton, 1992). Importantly, since contrastive methods only rely on consistency at the instance level, they do not require any spatial regularity between or within instances and are applicable to digital histopathology images. The consistency assumption has been exploited by Dosovitskiy, Springenberg, Riedmiller, and Brox (2014) to obtain a parametric feature representation for each training instance. Later, Wu, Xiong, Yu, and Lin (2018) extended Dosovitskiy et al. (2014) into a non-parametric feature representation using a dynamic memory bank to store latent features of data samples. The memory bank is used for selecting negative examples for each training instance, where any image that is not another view or augmentation of the original training instance is considered negative. The memory bank is then used to obtain negative samples without the need to recompute feature vectors. The use of simple image augmentations (e.g., resizing images, horizontal flips, color jittering, etc.) and memory banks have

proved successful in learning representations by maximizing the mutual information between latent representations of positives (Bachman, Hjelm, & Buchwalter, 2019; He, Fan, Wu, Xie, & Girshick, 2020; Hénaff et al., 2019). Data augmentations have also been utilized by applying the appropriate contrastive loss function on the feature vectors of positive and negative image pairs (Misra & Maaten, 2020; Tian, Krishnan, & Isola, 2019).

Recently, Chen, Kornblith, Norouzi et al. (2020) proposed a contrastive learning approach that does not require a custom network or a memory bank, but instead relies on using a large number of minibatch instances (≥ 256) for obtaining negative samples per training instance. By doing so, they were able to improve the quality of learned representations by providing more negative samples per training instance over training epochs. Along with a few architectural improvements, this method outperforms aforementioned techniques by a large margin (+7%) and has comparable performance to the supervised ResNet 50 network when its features are used in training a linear classifier for the ImageNet ILSVRC-2012 dataset (Russakovsky et al., 2015). This method was later incrementally improved by Grill et al. (2020) through techniques such as exponential moving averaging of the model weights (Tavainen & Valpola, 2017) or by knowledge distillation and using larger projection layers (Chen, Kornblith, Swersky, Norouzi, & Hinton, 2020). We choose not to explore these techniques in this paper as the added increase in performance (~4% in ImageNet top-1 accuracy) cannot be justified by the increase in the number of trainable parameters (e.g., ~800 million trainable parameters versus ~24 million).

3. The method

3.1. Contrastive self-supervised learning

We use the contrastive learning method proposed by Chen, Kornblith, Norouzi et al. (2020) which relies on maximizing agreement between representations of two stochastically augmented views of the same image (see Fig. 1). Specifically, given an image i , a probabilistic augmentation function $f_{\text{aug}}(\cdot)$, a neural network or an encoder $f_\theta(\cdot)$ with parameters θ and an auxiliary projection layer $p_{\hat{\theta}}(\cdot)$ with parameters $\hat{\theta}$, the aim is to match ℓ_2 normalized feature representations of two augmentations of the same image given by $z_i = p_{\hat{\theta}}(f_\theta(f_{\text{aug}}(i)))$. Simultaneously, other images in a batch are made dissimilar from the image i through a contrastive loss function called *NT-Xent* (the normalized temperature-scaled cross-entropy loss), defined as

$$\ell_{i,j} = -\log \frac{\exp(\text{similarity}(z_i, z_j)/\tau)}{\sum_{k=1}^{2N} \mathbb{1}_{[k \neq i]} \exp(\text{similarity}(z_i, z_k)/\tau)}, \quad (1)$$

where τ is the temperature parameter that helps weigh different examples to achieve hard negative mining, $\mathbb{1}$ is the indicator function which outputs 1 when $k \neq i$ and 0 otherwise, and the similarity function is a distance metric between two ℓ_2 normalized vectors. We refer to output of $f_\theta(\cdot)$ as the pre-activation layer output, and the output of $p_{\hat{\theta}}(\cdot)$ as the MLP output in Fig. 1, or z_i . The auxiliary projection layer is a single hidden layer MLP which is used to project the pre-activation layer output into a lower embedding space. Comparing z_i and z_j was found to be more effective in learning representations than directly comparing the pre-activation layer outputs. For our experiments, we use cosine similarity defined as $\text{similarity}(\mathbf{u}, \mathbf{v}) = \mathbf{u}^T \mathbf{v} / \|\mathbf{u}\| \|\mathbf{v}\|$. The authors experimentally find that NT-Xent helps learn better representations than similar loss functions such as margin (Schroff, Kalenichenko, & Philbin, 2015) or logistic (Mikolov, Chen, Corrado, & Dean, 2013) losses.

For each pretraining step with a batch size of $2N$, each augmented image has one similar (or positive) and $2(N-1)$ dissimilar (or negative) samples. By using samples in the same batch as negative samples, we avoid the expensive explicit negative example mining present in many methods He et al. (2020), Wu et al. (2018) and are able to scale up batch sizes where each pretraining step simultaneously optimizes for $\sim 4N^2$ feature vectors.

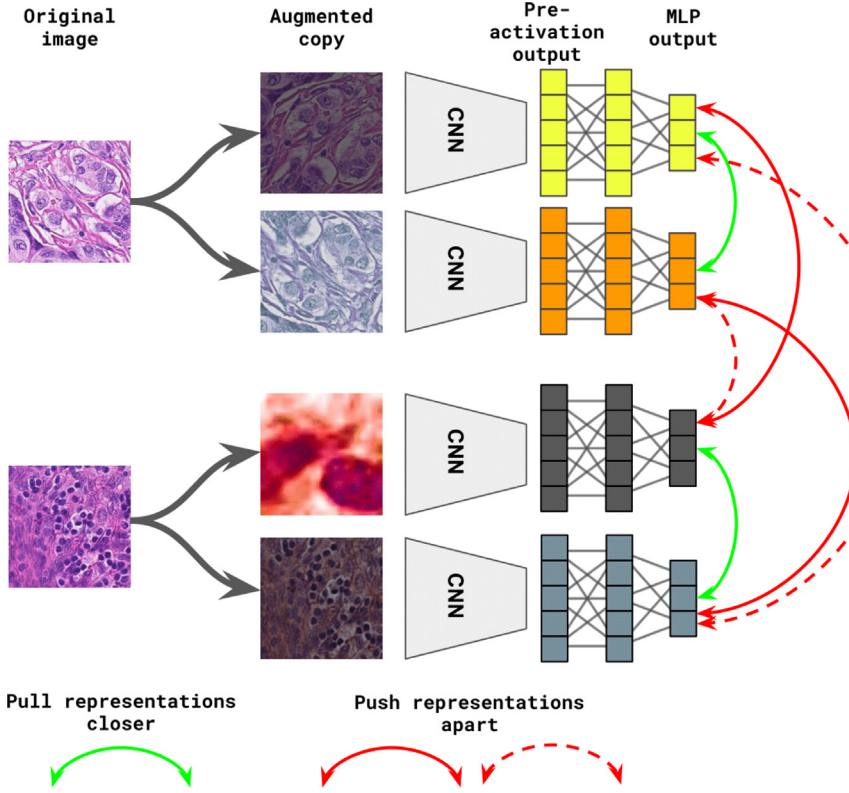


Fig. 1. Overview of the method. The block represented as *CNN* is identical for all image patches, and only replicated in the figure for clarity. We augment each image twice, extract features using the *CNN* at the pre-activation output, and transform these features into a lower embedding space at the multi-layer perceptron (*MLP*) output. While the augmented image patches from the same original source are pulled together (green arrows) in the feature space (at the *MLP* output), image patches from different sources are pushed apart using the NT-Xent loss function (both solid and dashed red arrows represent an identical push operation, shown as such in figure for clarity). The aim is to pretrain the network such that similarity between augmented views is used as a signal for learning salient features at the pre-activation layer. The figure is inspired from Chen, Kornblith, Norouzi et al. (2020).

Defining image diversity for histopathology. The contrastive method exploits the variability in visual properties between image patches to learn salient features. Obtaining visually diverse patches is challenging for digital histopathology, especially when images are viewed under high resolution. Given multiple unlabeled datasets, we assume that selecting images with different staining, resolution and tissue types will lead to a more diverse dataset compared to selecting image patches extracted from the same WSI or sampling images from the same dataset. In our early experiments, we found that pretraining with the dataset constructed using the former approach resulted in better validation performance than constructing a pretraining dataset where images are sampled from a single dataset. Furthermore, when images are inspected visually, the former approach exhibits more diversity (see Fig. 2).

4. Experiments

4.1. Pretraining datasets

Pretraining datasets include images from sites such as blood, breast, lymph, colon, bone, prostate, liver, pancreas, bladder, cervix, esophagus, head, neck, kidney, lung, thyroid, uterus, bone marrow, skin, brain, stomach, and ovary. Out of the total 57 datasets, 22 are comprised of image patches, 35 are WSI datasets. Most datasets are stained with hematoxylin and eosin (H&E) and come at the highest resolution of $0.25 \mu\text{m}/\text{pixel}$ (commonly referred to as $40\times$). While the majority of the WSI datasets are from The Cancer Genome Atlas Program (TCGA) and Clinical Proteomic Tumor Analysis Consortium (CPTAC) databases, we also use multiple public challenge datasets from lymph and breast cancer tasks. Image patch datasets are collected from various publicly available sources and exhibit similar organ diversity as WSI datasets. For the detailed list of pretraining datasets, please refer to Appendix F.1.

4.2. Validation experiments

Validation datasets. We validate pretrained networks trained under multiple settings (e.g., training only with a single dataset or tissue type, different number of training images etc.) on five classification, two segmentation and one regression dataset. The classification datasets include BACH (four class breast cancer classification), Lymph (three class malignant lymph node cancer classification), BreakHisv1 (binary breast cancer classification), NCT-CRC-HE-100K (nine class colorectal cancer tissue classification), and Gleason2019 (five class prostate cancer classification). Segmentation datasets are BACH (four class breast cancer segmentation on WSIs) and DigestPath2019 (WSI segmentation of early-stage colon tumors into healthy and cancerous tissue). Our single regression dataset is the BreastPathQ, which involves assigning a percentage cancer cellularity score to a given image patch. See Appendix C.1 for the detailed explanation of each validation set. In the following, abbreviations NCT, Bpq, and Dp19 refer to NCT-CRC-HE100K, BreastPathQ, and DigestPath2019, respectively.

Tasks. We compare pretrained networks with randomly initialized and ImageNet pretrained Resnet 18, 34, 50 and 101. For segmentation tasks, we use a UNet architecture (Ronneberger, Fischer, & Brox, 2015) which contains a pretrained encoder and a randomly initialized decoder. We compare two supervised training settings: fine-tuning and last layer training. In order to assess the learned representations directly, we freeze each residual network at the pre-activation layer and only train a linear classifier or a regressor on the learned representations (*last layer training*). The last layer supervised training setting is omitted for the segmentation task, since the UNet-like decoder (Yakubovskiy, 2020) that we use contains a comparable number of trainable parameters to the pretrained Resnet encoder, and can

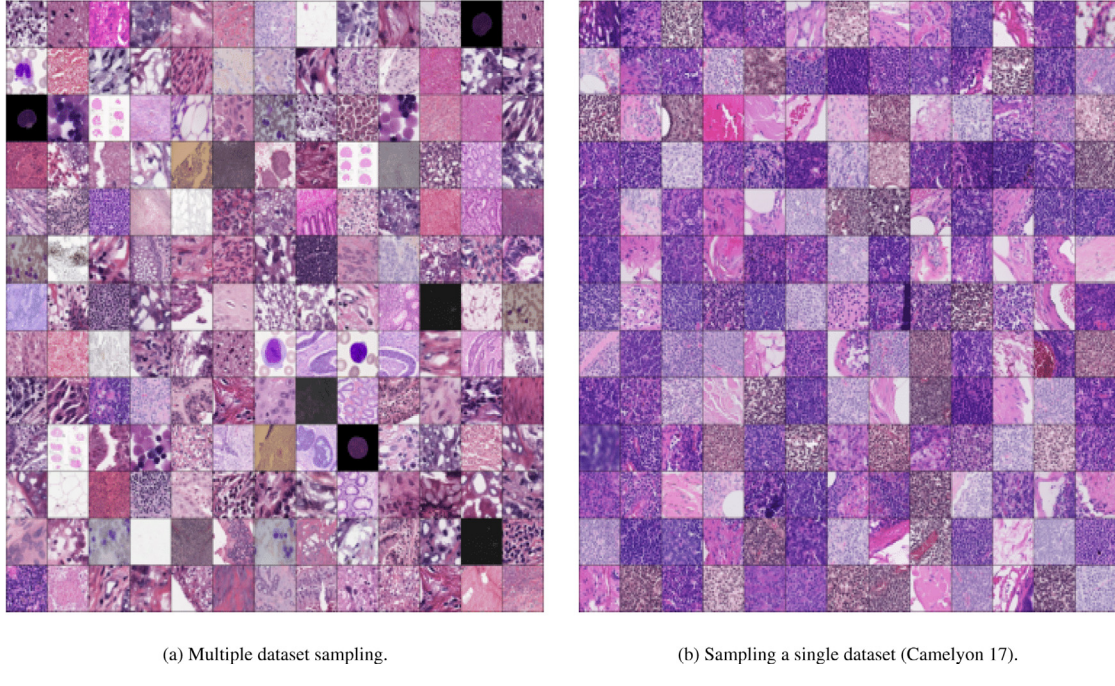


Fig. 2. Defining image diversity in the context of digital histopathology. Images evenly sampled from all 60 datasets visually look more diverse compared to sampling only from a single dataset containing multiple WSIs.

mitigate the benefits of using a pretrained encoder or ImageNet initialization. We also train each network without freezing any layers (*fine-tuning*). While fine-tuning is commonly employed, freezing various layers of a network may be used to avoid overfitting whenever the training dataset is small. Furthermore, pretrained features can also be used in clustering (see Section 5.3), feature selection, and in more traditional machine learning methods such as decision trees and support vector machines.

Validation setup. We train for 100 epochs per experiment, use Adam optimizer, a batch size of 128 with a weight decay of 0.00001 for Resnet18 models, and 0.0001 otherwise. We found that 100 epochs is enough for convergence for each validation dataset for all the networks (e.g., Resnet101) considered in this work. We use 50% of the original dataset as the training, 25% as validation, and 25% as the test set. We use macro F_1 score as our validation metric for the classification and segmentation tasks. Macro F1 weighs each class equally regardless of the number of samples per class, which accounts for the class imbalance seen in most digital histopathology datasets. For the regression task, we compute the mean absolute error (L_1) on the predictions and the ground truth regression labels (varying between 0 to 100%). The test metrics corresponding to the maximum validation metrics are reported. Please refer to the [Appendix A](#) for the definitions of evaluation metrics.

5. Results

Unless otherwise stated, all pretraining experiments are conducted with the Resnet18 model, and validation experiments were conducted without freezing any layers of the network. We use “pretraining” to refer to the unsupervised training. Pretrained networks are then used for “supervised” training on validation datasets. A dataset with half a million images of size 224×224 pixels can be pretrained for 1000 epochs using PyTorch on 4 T P100 GPUs in about 24 h for a Resnet 18 model. For a detailed explanation of augmentation and hyperparameter selection for the pretraining stage, please refer to [Appendix C](#).

In the following, we report the average classification and segmentation macro F_1 scores, as well as the L_1 error for the regression, in the appropriate subsection. The expanded results with individual datasets for each experiment are given in [Appendix D](#).

Table 1

The downstream task performance of networks trained on top of the pretraining, ImageNet initialization, and randomly initialized network (R denotes Resnet). We report F_1 score percentages (higher is better) averaged over five validation datasets for the classification task (Cls.), mean L_1 error difference (lower is better) between the ground truth and the predicted cellularity percentage for one dataset for regression (Reg.), and average two F_1 scores (higher is better) for segmentation (Seg.).

R	Pretrain.	Cl. [%]	Reg. [L_1]	Seg. [%]
18	Random	55.7	13.5	59.
	Imagenet	66.7	9.3	73.5
	Self sup.	77.0	6.6	74.0
34	Random	57.7	13.7	58.7
	Imagenet	65.7	7.1	66.2
	Self sup.	77.9	5.9	66.6
50	Random	55.3	13.3	58.8
	Imagenet	65.8	7.0	69.7
	Self sup.	76.9	5.5	66.7
101	Random	53.0	15.1	57.7
	Imagenet	67.0	6.7	69.
	Self sup.	76.2	5.3	65.9

5.1. Overall comparison

We compare networks pretrained with self supervision, ImageNet initialization, and randomly initialized networks for Resnet 18, 34, 50, and 101 in [Table 1](#). For comparison to other self- and unsupervised methods, please refer to [Appendix E](#).

We find that pretraining is superior to ImageNet on classification and regression tasks for all settings. Self supervision is comparable to ImageNet for segmentation in Resnet 18 and 34. For larger networks, ImageNet performs better.

5.2. Pretraining is most useful when only a small number of training images is available

It is generally accepted that pretrained networks boost the performance in medical image analysis ([Tajbakhsh et al., 2016](#)) and digital histopathology tasks ([Mehra et al., 2018](#)). We conduct validation experiments on the classification and regression tasks for all datasets

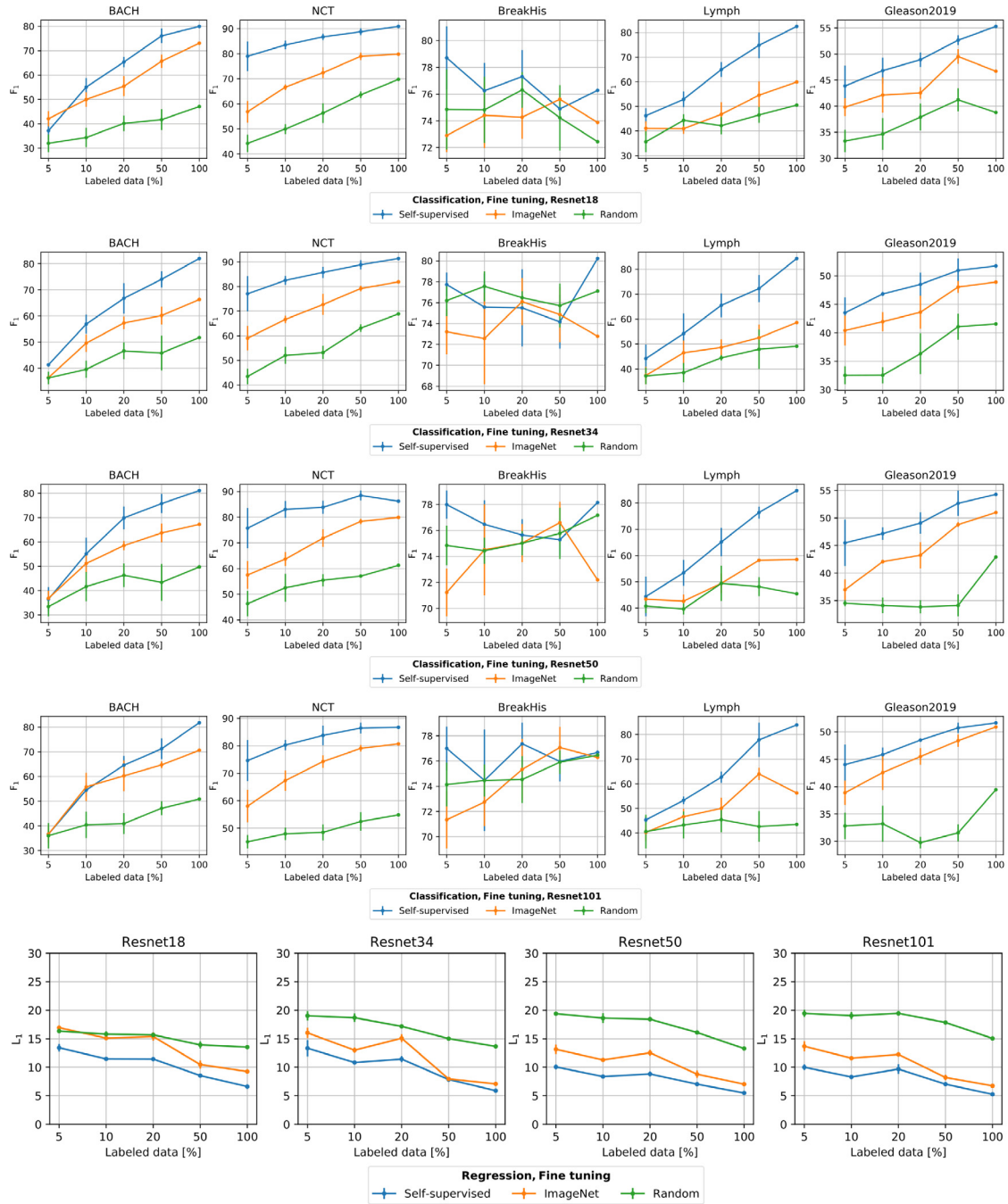


Fig. 3. Classification results showing the macro F_1 score on the five validation datasets, and the regression results showing the mean absolute error (L_1) on the BreastPathQ dataset for four differently sized Resnet models, when the supervised training was conducted without freezing any layers (fine tuning). We report the F_1 score and the L_1 error when $\{5, 10, 20, 50, 100\}\%$ of the labeled data is used for supervised training. Each percentage setting was run five times using different samples where the average and the standard deviation of five runs are shown as dots and error bars.

using $\{5, 10, 20, 50, 100\}\%$ of each training dataset, where for each percentage value we repeat experiments five times to obtain a better estimate of the performance. By limiting the amount of training data, we compare the effect of training dataset size on different pretraining settings. Specifically, we compare random initialization, ImageNet pre-training and self-supervised pre-training for networks Resnet 18, 34, 50 and 101. We report detailed results per dataset on Fig. 3.

We found that in the absence of a large training set, training a classifier or a regression network using a pretrained initialization can improve the performance. For instance, self supervision outperforms training from scratch (random setting) by over 40% for the NCT dataset when only 5% of the labeled images are used for training. When more

data is used, self supervision still remains superior to both ImageNet and random initializations.

5.3. Features obtained by pretraining are more representative for histopathological image patches than ImageNet features

We compare representations learned through self-supervision with the pretrained ImageNet features and randomly initialized residual network weights by training linear classifiers on the pre-activation layer of the Resnet models for the validation datasets. For Resnet 18 and Resnet 34, this amounts to 512 features, and to 2048 features for Resnet 50 and Resnet 101. We use 100% of the available data for each experiment. We

Table 2

The downstream task performance of linear classifiers trained on top of the learned features by self supervision, ImageNet initialization, and randomly initialized network. The network weights up to the pre-activation layer are frozen and not updated except for the linear classification layer. We report F_1 scores averaged over five validation datasets for the classification task, mean L_1 difference between the ground truth and the predicted cellularity percentage for one dataset for regression. Segmentation results using frozen encoders are omitted since a decoder can contain millions of parameters that can be trained to achieve satisfactory performance regardless of the encoder weights.

R	Pretrain.	Clss. [%]	Reg. [L_1]
18	Random	35.5	27.0
	Imagenet	41.1	14.9
	Self sup.	69.3	11.6
34	Random	35.0	29.3
	Imagenet	44.5	15.4
	Self sup.	67.6	13.5
50	Random	34.3	29.1
	Imagenet	46.4	12.0
	Self sup.	69.6	10.3
101	Random	27.2	2490.7
	Imagenet	45.0	12.9
	Self sup.	71.1	10.6

performed the same comparison for the regression task, where we froze the network at the pre-activation layer and trained a single regression layer. We do not include analogous frozen encoder experiments for the segmentation task since a decoder can contain millions of parameters that can be trained to achieve satisfactory performance regardless of the encoder weights. We report the average results in [Table 2](#), and the detailed results per dataset on [Fig. 4](#).

The self-supervised network achieves better results than ImageNet initialization, which indicates our method has learned domain-specific features that can be useful, especially when training samples are scarce. One may freeze and obtain features from various layers of the network for training various machine learning models, including neural networks, support vector machines or random forest classifiers.

Unsupervised clustering using the learned representations. Learned representations can be directly used for clustering without any labeled training examples. In this section, we use learned representations to cluster image patches extracted from WSIs. Note that the learned features can also be used for querying an image to its nearest neighbors without clustering the dataset, which is useful in applications such as active learning for sample selection and various data retrieval systems.

Negative mining is an important task in most tasks involving WSIs. For illustration of the saliency of learned representations, we perform negative mining on WSIs from a dataset including post-neoadjuvant therapy BRCA specimens with annotations of regions containing tumor ([Martel, Nofech-Mozes, Salama, Akbar, & Peikari, 2019](#); [Peikari, Salama, Nofech-Mozes, & Martel, 2017](#)). Randomly sampling patches from a WSI will result in a large class imbalance in favor of negatives, which leads to an increased ratio of false negatives. One may mitigate this issue by aggregating the sampled patches and selecting a subset of “representative” patches. This is done by clustering, where we rely on the perceived visual or morphological similarity of patches according to their relative distance to each other in the feature space. Specifically, we sample 1.4 million images from 69 WSIs and cluster images into three thousand clusters, where the number of clusters are determined using the Elbow heuristic ([Ciga et al., 2021](#)) (using the cluster sizes {1000, 1500, ..., 10000}, explained variance is 67.1% when 2500 clusters are used, 83.3% when 3000 clusters is used, and 91% when 5000 clusters is used), using their feature representations ($\in \mathbb{R}^{512}$) generated by the Resnet18 trained using self supervision. The features are clustered using the mini-batch K-means algorithm. The resulting clusters can be seen in [Fig. 5](#) with three samples per cluster. In addition, we select a few clusters and highlight them on WSIs to segment various regions of interests without any supervision in [Fig. 6](#).

Table 3

The effect of the number of images used for pretraining in the downstream task performance for classification, regression, and segmentation tasks. We report F_1 scores averaged over five validation datasets for the classification task, mean L_1 difference between the ground truth and the predicted cellularity percentage for one dataset for regression, and average two F_1 scores for segmentation.

% of images	Clss. [%]	Reg. [L_1]	Seg. [%]
0.01%	66.5	8.5	62.7
0.1%	73.9	7.8	72.8
1%	77.0	6.8	70.8
10%	79.1	6.6	73.5

Table 4

Examining the impact of resolution on task performance. We use images from one resolution for pretraining and evaluate the pretrained network on all available validation datasets. 10x, 20x, and 40x refer to 1 $\mu\text{m}/\text{pixel}$, 0.50 $\mu\text{m}/\text{pixel}$, and 0.25 $\mu\text{m}/\text{pixel}$, respectively. We report F_1 scores averaged over five validation datasets for the classification task, mean L_1 difference between the ground truth and the predicted cellularity percentage for one dataset for regression, and average two F_1 scores for segmentation.

Resolution	Clss. [%]	Reg. [L_1]	Seg. [%]
10x	61.0	10.9	56.5
20x	60.5	9.9	57.6
40x	65.4	9.4	62
10, 20, 40x	67.0	9.3	63

5.4. Using more unlabeled images in pretraining improves the downstream task performance

Extracting patches of size 224×224 pixels from WSIs that contain foreground (refer to [Appendix B](#)) can lead to a few million patches per dataset, which can quickly become intractable. Therefore, we randomly sample a maximum of 100 patches from each WSI and use all images from non-WSI datasets to generate the unsupervised pretraining data. We use the maximum available resolution per WSI, which is $\sim 0.25 \mu\text{m}/\text{pixel}$ or $\sim 0.50 \mu\text{m}/\text{pixel}$ depending on the dataset. We use 206 thousand images from 23 non-WSI datasets and sample over four million patches from 35 WSI datasets containing around 25 thousand WSIs. We compare using {0.01, 0.1, 1, 10}% of the sampled datasets with a maximum of two thousand and a minimum of 10 images per dataset if the number of images corresponding to the percentage setting for a dataset is below 10. In the end, we obtain 4, 40 and 400 thousand images per percentage setting. In addition, we pretrain a model using only 10 images per dataset ($\sim 0.01\%$ of all available images). In this setting, we sample 10 image patches from each WSI dataset as well, which can contain a few million image patches across all WSIs in that dataset. Therefore, the dataset is drastically undersampled. The results can be seen in [Table 3](#).

We found that using a larger training set outperforms using a training set with fewer images. Notably, we observe diminishing returns with every order of magnitude of increase in dataset size. While the difference between using 0.01% and 0.1% of the available images is 7.4% in average F_1 for the classification task, the difference between 1% and 10% is around 2.1%.

5.5. The impact of resolution on the pretraining

To assess the impact of resolution on the learned features, we pretrain four networks using images at different resolutions. We use a breast image dataset, originally aimed to identify the invasive ductal carcinoma grade at multiple resolutions ([Bolhasani, Amjadi, Tabatabaeian, & Jassbi, 2020](#)). In the results shown in [Table 4](#), 10x, 20x, and 40x refer to 1 $\mu\text{m}/\text{pixel}$, 0.50 $\mu\text{m}/\text{pixel}$, and 0.25 $\mu\text{m}/\text{pixel}$, respectively. We pretrain networks using images with resolutions 10x, 20x, and 40x, in addition to using all available images (10, 20, 40x).

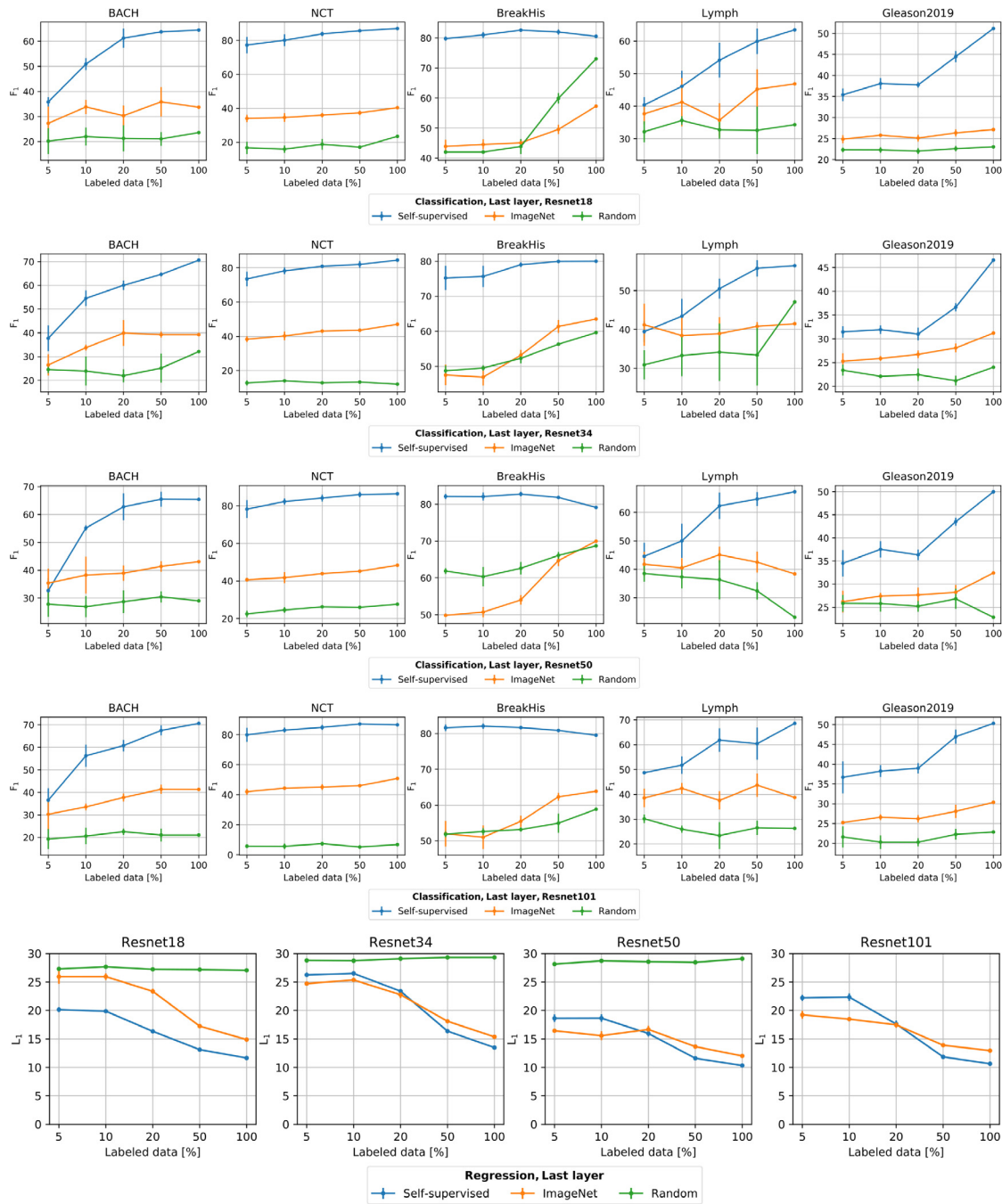


Fig. 4. Classification results showing the macro F_1 score on the five validation datasets, and the regression results showing the mean absolute error (L_1) on the BreastPathQ dataset for four differently sized Resnet models, when the supervised training was conducted by freezing all the layers except the linear classification or the linear regression layer (last layer setting). We report the F_1 score when {5, 10, 20, 50, 100}% of the labeled data is used for supervised training. Each percentage setting was run five times using different samples where the average and the standard deviation of five runs are shown as dots and error bars. For the Resnet 101, last layer training, randomly initialized network's error is too large to fit in the plot.

We find that the networks pretrained on images at higher resolutions tend to perform better in downstream tasks. Furthermore, we find that combining multiple resolutions further improves task performances.

5.6. Transferability of features between tissue types and staining

To assess if it is better to pretrain using datasets drawn exclusively from a similar tissue type to that present in the target task, we conducted separate experiments using Resnet 18 with three different tissue types: breast, lymph nodes and prostate. Specifically, we trained a

network using only Camelyon 16 and Camelyon 17 datasets for lymph nodes, and TCGA-PRAD and Prostate-MRI datasets for prostate. Due to the greater availability of data for breast, we trained on a larger number of datasets: TCGA-BRCA, TUPAC16, TNBC, several datasets from Andrew Janowczyk, ICPR2014 and ICPR2012 (see Table F.13 for dataset descriptions). For each experiment, roughly the same number of training images were used (~ four thousand). The results can be viewed in Table 5.

Despite the site-specific pretraining (i.e., the tissue used in pretraining), we did not observe a strong correlation between the pretrained model and the validation performance. For instance, prostate models

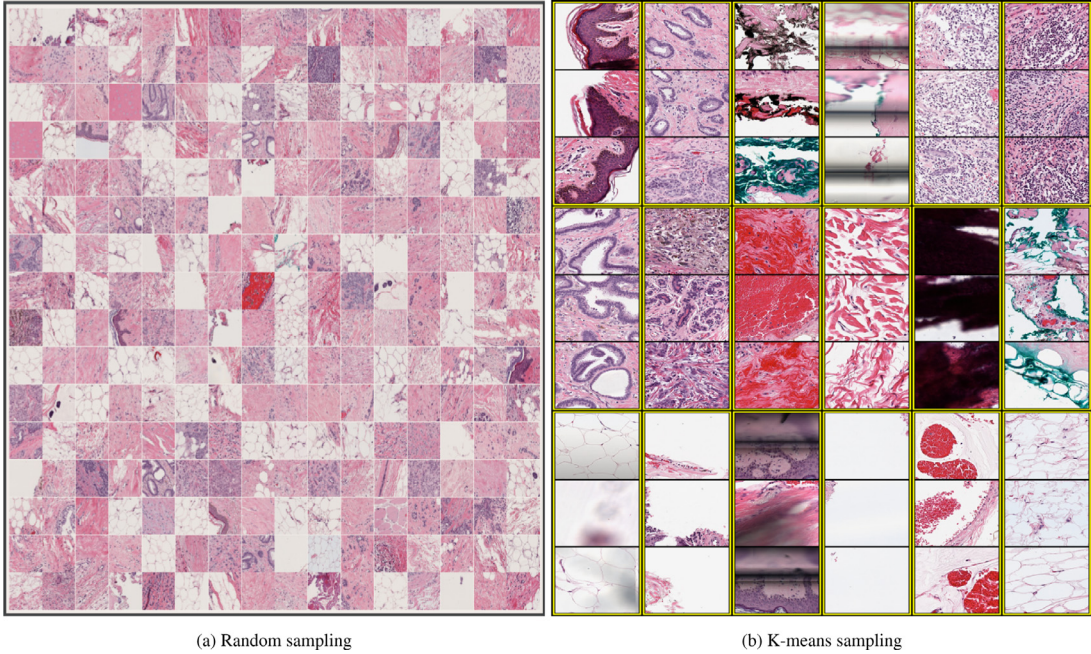


Fig. 5. Sampling image patches from whole-slide images randomly versus feature based K-means clustering. Each figure is extracted from an actual experiment. In Fig. 5(b), each yellow box shows three samples closest to the center of a randomly selected cluster for illustration. Note that visually similar patches with features such as out-of-focus regions, creases, ink marks of different colors, morphological structures such as ducts, outlines of the nipple, and red blood cells are clustered together. Furthermore, patches with varying nuclei formation patterns are also clustered roughly according to their density. (For interpretation of the references to color in this figure legend, the reader is referred to the web version of this article.)

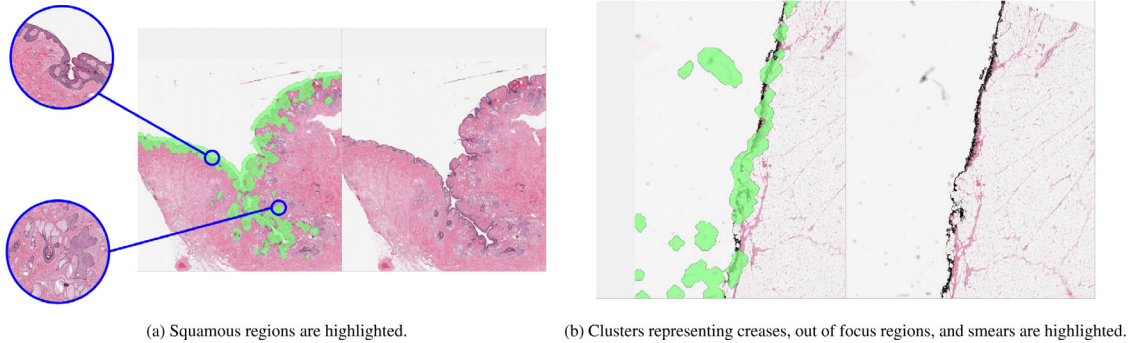


Fig. 6. A practical application of unsupervised clustering in digital histopathology. We first cluster 1.4 million feature vectors corresponding to image patches into three thousand clusters without any supervision. Then, these clusters are used to highlight different regions of interest on whole-slide images.

Table 5

Examining the transferability of features between organs. We use images from one organ for pretraining and validate it on all available validation datasets. We report F_1 scores averaged over five validation datasets for the classification task, mean L_1 difference between the ground truth and the predicted cellularity percentage for one dataset for regression, and average two F_1 scores for segmentation.

Tissue	Classification [%]						Regression [L_1]		Segmentation [%]		
	BACH	NCT	BreakHis	Lymph	Gleason2019	Average	Bpq	BACH	Dp19	Average	
Breast	75.	86.	79.1	73.8	47.3	72.2	7.5	49.0	84.9	67.0	
Lymph	75.1	83.1	76.	70.6	48.4	70.6	8.2	48.0	83.3	65.7	
Prostate	78.3	80.6	75.4	65.9	54.7	71.0	8.7	56.5	84.5	70.5	

outperformed breast models on the BACH dataset for both breast cancer classification and segmentation. Similarly, the lymph model was outperformed by the breast model on the malignant lymph cancer detection. However, it should be noted that for some datasets the site-specific pretraining yielded better performance. For instance, breast model performed the best on the BreastPathQ dataset, and prostate model outperformed other models on the Gleason prostate cancer grading. In addition, we observed poorer performance compared to training with all datasets, where the results in Tables 1 and D.7 indicate using images from a more diverse pretraining dataset with comparable

number of pretraining images leads to better performance across all tasks.

6. Discussion

In Section 5.1, we have observed that the self supervision performs better than the ImageNet initialization for the *segmentation task* for Resnet 18 and 34. In contrast, for Resnet 50 and 101, ImageNet performs better. We hypothesize this is due to the increased number

of trainable parameters for the decoder, diminishing the effect of pretraining the encoder.

In Section 5.6, we have observed that the tissue type used as data for pretraining was not correlated to the downstream task performance on the validation datasets. We believe the lack of correlation and the degradation compared to using all tissue types can be due to the following factors: (1) limitations of the contrastive approach where representations are incapable of encoding domain-specific information in the absence of the *other tissue types*, (2) convolutional networks are highly sensitive to visual properties such as staining, resolution and morphological shapes, and do not encode abstract features in the absence of a specific objective (e.g., cancer grading), (3) the network can only be *incentivized* to encode a richer representation given a diverse pretraining dataset.

7. Conclusion

Our main objective in this work was to show that, by pretraining, we can learn better features to improve performances on multiple downstream tasks, including classification, regression, and segmentation. The self-supervised method outlined in this paper is the first method to consistently have comparable performance to ImageNet pretraining without additional complexity. To our knowledge, there is no prior research on histopathological image analysis with a training regimen that consistently reaches or surpasses supervised training. In addition, this is the first study which uses a very large number of images in digital histopathology setting: 23 image datasets with over 206 thousand patches and ~25 thousand gigaresolution images in 35 datasets that consist of whole-slide images.

We have shown that the success of the contrastive pretraining method heavily relies on the diversity of the unlabeled training set, as opposed to the number of images. This is an important consideration when one adopts a technique from the computer vision community, where most methods are validated on natural scene images that contain significantly more diversity than medical images. Furthermore, we have shown that the site which the training images were extracted from did not have a substantial effect on the quality of learned representations, as shown in Section 5.6. While this shows a clear divergence from the training of human experts who focus on a specific organ, it also can significantly increase the number of available datasets in training such systems.

In this work, we focused on the simplest contrastive method which significantly improved the state-of-the-art and experimented under multiple settings outlined in Section 4 to understand the capabilities and limitations of the contrastive training for histopathology images. We believe that so long as the fundamentals of the sample contrastive training framework remain the same, the insights we obtained will still be valid for future work on self-supervision. Overall, we found that contrasting images which are visually distinguishable helped in learning salient representations. In contrast, images which look similar with small nuances that are important in histopathology (e.g., single cell tumors that only occupy a small portion of a given patch) were not suitable for contrastive learning, and led to noisy representations. As this is rarely the case for the natural-scene images, researchers working on digital histopathology images need to address domain-specific issues to bridge the gap between histopathology and computer vision in self-supervised learning.

CRediT authorship contribution statement

Ozan Ciga: Conceptualization, Methodology, Software, Data curation, Writing - original draft, Visualization, Validation. **Tony Xu:** Software, Writing - original draft, Validation. **Anne Louise Martel:** Supervision, Investigation, Writing - review & editing.

Declaration of competing interest

The authors declare that they have no known competing financial interests or personal relationships that could have appeared to influence the work reported in this paper.

Acknowledgments

This work was funded by Canadian Cancer Society (grant #705772) and Natural Sciences and Engineering Research Council (NSERC) (grant # RGPIN-2016-06283). It was also enabled in part by support provided by Compute Canada (www.computecanada.ca). The results shown here are in part based upon data generated by The Cancer Genome Atlas (TCGA) Research Network: <https://www.cancer.gov/tcga>, and the Clinical Proteomic Tumor Analysis Consortium (CPTAC): <https://cptac-data-portal.georgetown.edu/cptacPublic/>.

Appendix A. Evaluation metrics

$$\frac{tp}{tp + fp} \quad \text{precision} \quad (\text{A.1})$$

$$\frac{tp}{tp + fn} \quad \text{recall} \quad (\text{A.2})$$

$$\frac{precision \cdot recall}{(precision + recall)/2} \quad F1 \text{ score} \quad (\text{A.3})$$

tp stands for true positive, fp is false positive and fn is false negative. We use macro F_1 score in reporting classification and segmentation results. Macro F_1 assigns the same weight to each class-wise score prior to averaging over all classes to take the class imbalance present in most of our validation datasets into account.

We use the L_1 error for the regression task. L_1 is defined as the mean absolute difference (MAD) between ground truth (gt_i) and the prediction (pred) over N samples, or $\sum_{i=1}^N |gt_i - pred_i|$. The subscript i indexes the ground truth and prediction belonging to sample i .

Appendix B. Foreground filtering

Due to their immense size, WSIs contain many regions that may be irrelevant for histopathology, such as ink, creases, fat, and white background. We threshold each WSI in HSV color space, with the following threshold parameters: $0.65 > hue > 0.5$, $saturation > 0.1$, and $0.9 > value > 0.5$. The bounds are experimentally determined using a public breast cancer segmentation dataset ([Aresta et al., 2019](#)) to isolate the irrelevant background regions. Each WSI is tiled into patches of size 224×224 pixels, and patches with foreground ratios $\geq 50\%$ are used as unsupervised training data.

Appendix C. Hyperparameter and suitable augmentation selection

Setup. We conduct experiments to determine the best hyperparameter setting for histopathology images. We pretrain a Resnet 18 using ~40 thousand images sampled from 57 unlabeled datasets. We use the average macro F1 metric on five validation datasets for the classification task to select each hyperparameter. We compare temperatures {0.05, 0.1, 0.5, 1, 2, 10} and batch sizes {128, 256, 512}. We compare Adam ([Kingma & Ba, 2014](#)), Lars ([You, Gitman, & Ginsburg, 2017](#)), and Lamb ([You et al., 2019](#)) optimizers to account for the large batch size. We use learning rates $0.3 \times \frac{batchsize}{256}$, $\frac{4}{2^{(3-(log_2(batchsize)-9)/2)} \times 100}$, and 10^{-4} for Lars, Lamb, and Adam, respectively (as proposed by [Chen, Kornblith, Norouzi et al. \(2020\)](#) for Lars and by [You et al. \(2017\)](#) for Lamb). We use 10^{-6} as the weight decay.

Since the original set of augmentations were applied on natural-scene images, they may not be suitable for histopathology. We conduct ablation studies on data augmentations with minor modifications. For instance, the original paper uses 8% to 100% randomly resized crops,

Table C.6

Comparison between Lars and Lamb optimizers used for large batch pretraining a self-supervised network. In optimizer selection experiments, we use baseline augmentations which consist of $\in \{0^\circ, 90^\circ, 180^\circ, 270^\circ\}$ image rotations, flips in each axis with 50% probability, Gaussian blurring, and light color jittering. Results are shown in macro F_1 scores.

Optimizer	Temperature	BACH	NCT	BreakHis	Lymph	Gleason2019	Average
Lars	0.05	77.2	87.2	73.9	73.2	49.8	72.2
	0.10	80.3	82.7	73.9	80.9	51.7	73.9
	0.50	73.9	81.3	75.5	69.2	51.9	70.4
Lamb	0.05	74.7	83.5	67.8	74.1	53.7	70.8
	0.10	79.6	84.1	71.4	71.9	51.9	71.8
	0.50	69.7	82.7	78.	75.4	48.	70.8

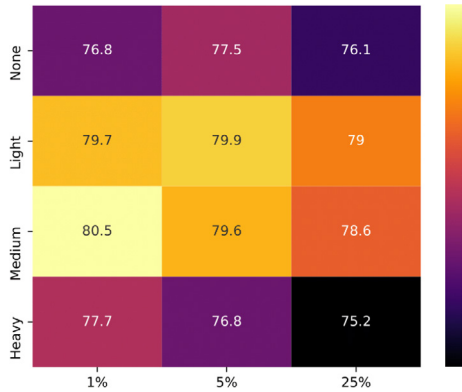


Fig. C.7. Different combinations of color jittering and random cropping. The figures represent the macro F_1 scores averaged over five validation datasets. (For interpretation of the references to color in this figure legend, the reader is referred to the web version of this article.)

whereas we compare minima {1%, 5%, 25%}, with 100% as the maximum in all settings. We train for 1000 epochs per experiment. Since loss is a function of the temperature, performance cannot be assessed by comparing different values of the loss. Therefore each pretrained network is assessed on independent validation datasets.

Data augmentations. In our experiments, we employ randomly resized crops, 90° rotations, horizontal and vertical flips, photometric manipulation (color jittering) and Gaussian blurring as augmentations. We randomly select a rectangle corresponding to 1 to 100% of the area of the original image patch and resize it to the original image's size, stochastically rotate images with degrees $\in \{0^\circ, 90^\circ, 180^\circ, 270^\circ\}$ with equal (25%) probability, flip in each axis with 50% probability, and compare color jittering strategies where we adjust (brightness, contrast, saturation, hue) of a given image by a percentage value of the original image. Specifically, we compare three types of jittering augmentations

with different strengths: light (brightness=0.4, contrast=0.4, saturation=0.4, hue=0.2), medium (0.8, 0.8, 0.8, 0.2) and heavy (0.8, 0.8, 0.4). Each number in parentheses represents the fraction of possible change in the corresponding color property, e.g., $\pm 40\%$ shift in brightness in the light jittering augmentation setting. A 100% change in brightness can mean a fully dark image (0% brightness) or doubling the brightness value (200%). Finally, we employ Gaussian blurring 50% of the time, with standard deviation $\sigma \sim \mathcal{U}[0.1, 2.0]$ and kernel size $0.1 \times$ image patch's side length.

Results. In our initial experiments, we observed Adam did not converge for batch sizes ≥ 256 and was discarded. A batch size of 512 performed the best for both optimizers for all temperature values and is used in all the subsequent experiments. Lamb is a newer technique where [You et al. \(2019\)](#) have shown better large batch training performance with faster convergence on convolutional networks. However, we observed Lars outperformed Lamb in most settings and was therefore used for the remaining experiments. We found smaller temperatures generally performed better, and larger ones (1, 2, 10) did not converge. The temperature parameter of 0.1 performed the best for both optimizers. For the complete list of experiments, please refer to [Table C.6](#).

Interestingly, we found that randomly cropping 1% of the image patch and resizing to its original size outperformed both 5% and 25% for medium and heavy color jittering settings. We found color jittering strongly correlated with the quality of learned representations. No color jittering has the lowest training loss since it is easy to distinguish images without tampering with their color properties. However, it was outperformed by both light and heavy jittering settings. Overall, we observed that more aggressive augmentations resulted in better representations. For instance, while 1% of a 224×224 patch (a 2×2 square) cannot be used to distinguish the original patch it was extracted from, it still outperformed {5%, 25%} for the medium jittering setting, which performed the best across all settings by over 0.6% over the next best setting in F_1 . We argue that the improvement is due to a regularization effect on the contrastive objective, which prevents saturation and enables the learning of more salient features. The average F_1 scores obtained from a combination of different augmentation and random cropping settings are shown in [Table D.11](#) (see [Fig. C.7](#)).

Table D.7

The downstream task performance of networks trained on top of the pretraining, ImageNet initialization, and randomly initialized network. We report F_1 scores averaged over five validation datasets for the classification task, mean L_1 difference between the ground truth and the predicted cellularity percentage for one dataset for regression, and average two F_1 scores for segmentation. Column with the header R indicates the Resnet model, and Reg. stands for regression.

R	Pretraining	Classification [%]						Reg. [L_1]	Segmentation [%]		
		BACH	NCT	BreakHis	Lymph	Gl19	Average		Bpq	BACH	Dp19
18	Random	47.1	69.7	72.4	50.5	38.8	55.7	13.5	42.8	75.1	59.0
	ImageNet	73.1	79.8	73.9	59.9	46.7	66.7	9.3	60.5	86.6	73.6
	Self supervised	80.0	90.9	76.3	82.5	55.3	77.0	6.6	61.9	86.0	74.0
34	Random	66.3	81.9	72.8	58.6	48.9	65.7	13.7	40.7	76.8	58.8
	ImageNet	74.3	80.1	71.1	70.4	45.3	68.2	7.1	45.2	87.1	66.2
	Self supervised	82.0	91.4	80.2	84.3	51.8	77.9	5.9	47.2	86.0	66.6
50	Random	49.8	61.2	77.2	45.4	42.9	55.3	13.3	44.1	73.6	58.9
	ImageNet	67.3	79.9	72.2	58.5	51.0	65.8	7.0	51.9	87.4	69.7
	Self supervised	81.1	86.2	78.2	84.8	54.3	76.9	5.5	46.7	86.6	66.7
101	Random	50.9	54.8	76.5	43.5	39.4	53.0	15.1	41.4	74.0	57.7
	ImageNet	70.6	80.7	76.3	56.3	50.9	67.0	6.7	50.7	87.4	69.1
	Self supervised	81.8	86.7	76.7	83.9	51.6	76.2	5.3	46.0	85.8	65.9

Table D.8

The downstream task performance of linear classifiers trained on top of the learned features by self supervision, ImageNet initialization, and randomly initialized network. We report F_1 scores averaged over five validation datasets for the classification task, mean L_1 difference between the ground truth and the predicted cellularity percentage for one dataset for regression, and average two F_1 scores for segmentation. Column with the header R indicates the Resnet model.

R	Pretraining	Classification [%]						Regression [L_1]
		BACH	NCT	BreakHis	Lymph	Gleason2019	Average	
18	Random	23.6	23.5	73.1	34.3	23.0	35.5	27.0
	ImageNet	33.7	40.3	57.3	46.9	27.1	41.1	14.9
	Self supervised	64.5	87.0	80.6	63.5	51.2	69.3	11.6
34	Random	32.1	12.1	59.6	47.1	24.0	35.0	29.3
	ImageNet	39.3	47.1	63.5	41.5	31.2	44.5	15.4
	Self supervised	70.6	84.5	80.0	56.4	46.6	67.6	13.5
50	Random	29.1	27.7	68.7	23.1	22.8	34.3	29.1
	ImageNet	43.1	48.3	70.0	38.4	32.4	46.4	12.0
	Self supervised	65.4	86.4	79.1	67.3	50.0	69.6	10.3
101	Random	21.0	6.8	58.8	26.3	22.8	27.2	2490.7
	ImageNet	41.3	50.8	63.9	38.8	30.4	45.0	12.9
	Self supervised	70.6	86.5	79.5	68.6	50.3	71.1	10.6

Table D.9

Examining the impact of resolution on task performance. We use images from one resolution for pretraining and evaluate the pretrained network on all available validation datasets. 10x, 20x, and 40x refer to 1 $\mu\text{m}/\text{pixel}$, 0.50 $\mu\text{m}/\text{pixel}$, and 0.25 $\mu\text{m}/\text{pixel}$, respectively. We report F_1 scores averaged over five validation datasets for the classification task, mean L_1 difference between the ground truth and the predicted cellularity percentage for one dataset for regression, and average two F_1 scores for segmentation.

Resolution	Classification [%]						Reg. [L_1]	Segmentation [%]		
	BACH	NCT	BreakHis	Lymph	Gleason2019	Average		Bpq	BACH	Dp19
10x	62.8	69.0	78.6	50.6	43.9	61.0	10.9	37.8	75.1	56.5
20x	54.6	65.7	74.2	65.4	42.7	60.5	9.9	42.4	72.8	57.6
40x	66.1	73.8	73.3	69.2	44.4	65.4	9.4	42.4	81.6	62
10, 20, 40x	65.1	74.0	75.3	76.9	43.7	67.	9.3	42.2	83.9	63.0

Table D.10

The effect of the number of images used for pretraining in the downstream task performance for classification, regression, and segmentation tasks. We report F_1 scores averaged over five validation datasets for the classification task, mean L_1 difference between the ground truth and the predicted cellularity percentage for one dataset for regression, and average two F_1 scores for segmentation.

% of images	Classification [%]						Reg. [L_1]	Segmentation [%]		
	BACH	NCT	BreakHis	Lymph	Gleason2019	Average		Bpq	BACH	Dp19
0.01%	65.1	77.6	75.4	62.8	51.6	66.5	8.5	43.4	81.9	62.7
0.1%	77.7	85.0	78.6	75.2	53.0	73.9	7.8	61.0	84.5	72.8
1%	80.0	90.9	76.3	82.5	55.3	77.0	6.8	55.7	85.9	70.8
10%	87.0	89.9	75.4	90.1	53.1	79.1	6.7	60.8	86.2	73.5

Table D.11

Selecting suitable augmentations for self-supervised learning on digital histopathology tasks. Baseline augmentations consist of $\{0^\circ, 90^\circ, 180^\circ, 270^\circ\}$ image rotations, flips in each axis with 50% probability, Gaussian blurring, and light color jittering. Results are shown in macro F_1 scores.

Random crop	Augmentation intensity	BACH	NCT	BreakHis	Lymph	Gleason2019	Average
1%	None	75.9	89.	79.5	87.1	52.3	76.8
	Light	81.7	93.6	82.7	88.	52.3	79.7
	Medium	84.4	94.4	80.7	88.2	54.8	80.5
	Heavy	82.4	93.1	77.2	78.1	54.2	77.0
5%	None	78.	88.7	78.9	87.1	54.9	77.5
	Light	82.4	94.2	80.8	88.1	53.8	79.9
	Medium	85.3	93.8	81.	83.9	54.2	79.6
	Heavy	82.5	93.2	77.4	78.4	52.6	76.8
25%	None	66.5	77.1	74.7	71.3	53.5	68.6
	Light	69.7	82.7	78.	75.4	48.	70.8
	Medium	73.9	81.3	75.5	69.2	51.9	70.4
	Heavy	81.9	92.6	75.7	73.7	52.2	75.2

Table E.12

Comparison of different self-supervised techniques. Each method uses the Resnet50 architecture as its encoder.

Setting	Classification [%]						Regression [L_1]	Segmentation [%]		
	BACH	NCT	BreakHis	Lymph	Gleason2019	Average		Bpq	BACH	Dp19
Ours	81.1	86.2	78.2	84.8	54.3	76.9	5.5	46.7	86.6	66.7
CPCv2	74.3	80.1	71.1	70.4	45.3	68.2	7.8	41.1	75.3	58.2
Colorization	69.2	80.2	72.4	60.0	50.5	66.5	12.2	40.9	74.1	57.5
Autoencoder	29.2	37.0	36.0	26.1	22.9	30.2	11.7	28.8	52.9	40.9

Table F.13

Datasets used for pretraining models.

Image patch datasets					
Dataset	Organ	Resolution	Staining	Number of patches	Image type
AML-Cytomorphology LMU (Matek, Schwarz, Spiekermann, & Marr, 2019)	Blood	100x	Wright's stain	18365	Patch
andrewjanowczyk epi (Janowczyk & Madabhushi, 2016)	Breast	20x	H&E	125	Patch
andrewjanowczyk lymphoma (Janowczyk & Madabhushi, 2016)	Various	40x	H&E	374	Patch
andrewjanowczyk mitosis (Janowczyk & Madabhushi, 2016)	Breast	40x	H&E	311	Patch
andrewjanowczyk nuclei (Janowczyk & Madabhushi, 2016)	Breast	40x	H&E	142	Patch
andrewjanowczyk tubule (Janowczyk & Madabhushi, 2016)	Colorectal	40x	H&E	85	Patch
C-NMC training data (Gehlot, Gupta, & Gupta, 2019)	Blood, bone	Unknown	H&E	10661	Patch
CoNSeP (Graham et al., 2019)	Colon	40x	H&E	41	Patch
CRCHistoPhenotypes (Sirinukunwattana et al., 2016)	Colorectal	20x	H&E	200	Patch
Pannuke Fold 1 (Gamper, Koohbanani, Benet, Khuram, & Rajpoot, 2019)	Various	Various	H&E	2656	Patch
glas 2015 (Sirinukunwattana et al., 2016)	Colon	20x	H&E	165	Patch
icpr 2014 (Capron, Calvo, Attieh, Naour, & Gloaguen, 2014)	Breast	20, 40x	H&E	3975	Patch
icpr 2012 (Roux et al., 2013)	Breast	40x	H&E	100	Patch
lyon2019 (Swiderska-Chadaj et al., 2019)	Breast, colon, prostate	40x	Anti CD3, CD8	441	Patch
MiMM SBILab (Gupta, 2018)	Bone	100x	Jenner-Giemsa	85	Patch
MoNuSeg Training Data (Kumar et al., 2020)	Various	40x	H&E	30	Patch
Prostate-MRI (Choyke, Turkbey, Pinto, Merino, & Wood, 2016)	Prostate	Unsure	H&E	26	Patch
ramtab (Raza et al., 2012)	Colon	Unsure	Various fluorescence	200	Patch
SN-AM B-ALL and MM (Gupta & Gupta, 2019)	Blood, bone	100x	Jenner-Giemsa	61	Patch
TNBC NucleiSegmentation (Jack, Thomas, Marick, & Fabien, 2018)	Breast	40x	H&E	50	Patch
warwick beta cell dataset (Kuse, Wang, Kalasannavar, Khan, & Rajpoot, 2011)	Pancreas	40x	H-DAB	20	Patch
IDCGrade (Bolhasani et al., 2020)	Breast	10x,20x,40x	H&E	922	Patch
Whole-slide datasets					
Dataset	Organ	Resolution	Staining	Number of WSIs	Image type
TCGA-BLA	Bladder	40x	H&E	469	WSI
TCGA-BRCA	Breast	20, 40x	H&E	1987	WSI
TCGA-CESC	Cervix	40x	H&E	327	WSI
TCGA-COAD	Colon	20, 40x	H&E	983	WSI
TCGA-ESCA	Esophagus	20, 40x	H&E	260	WSI
TCGA-GBM	Brain	20, 40x	H&E	1193	WSI
TCGA-HNSC	Head, neck	20, 40x	H&E	791	WSI
TCGA-KICH	Kidney	20, 40x	H&E	275	WSI
TCGA-KIRC	Renal	20, 40x	H&E	1656	WSI
TCGA-KIRP	Renal	20, 40x	H&E	475	WSI
TCGA-LGG	Brain	40x	H&E	728	WSI
TCGA-LIHC	Liver	20, 40x	H&E	492	WSI
TCGA-LUAD	Chest	20, 40x	H&E	1067	WSI
TCGA-LUSC	Lung	20, 40x	H&E	1100	WSI
TCGA-OV	Ovary	20x	H&E	1376	WSI
TCGA-PRAD	Prostate	20, 40x	H&E	736	WSI
TCGA-READ	Rectum	20, 40x	H&E	364	WSI
TCGA-SARC	Various	20, 40x	H&E	290	WSI
TCGA-STAD	Stomach	20, 40x	H&E	771	WSI
TCGA-THCA	Thyroid	20, 40x	H&E	639	WSI
TCGA-UCEC	Uterus	20, 40x	H&E	805	WSI
CPTAC-AML	Marrow, blood	40x	PAS, Wright	123	WSI
CPTAC-CCRCC	Kidney	20x	H&E	783	WSI
CPTAC-CM	Skin	20x	H&E	402	WSI
CPTAC-GBM	Brain	20x	H&E	508	WSI
CPTAC-HNSCC	Head, neck	20x	H&E	390	WSI
CPTAC-LSCC	Lung	20x	H&E	1073	WSI
CPTAC-LUAD	Lung	20x	H&E	1065	WSI
CPTAC-PDA	Pancreas	20x	H&E	557	WSI
CPTAC-UCEC	Uterus	20x	H&E	887	WSI
camelyon16 (Ehteshami Bejnordi et al., 2017)	Lymph node	40x	H&E	400	WSI
tupac16 (Veta et al., 2019)	Breast	40x	H&E	821	WSI
camelyon17 (Litjens et al., 2018)	Lymph node	40x	H&E	1000	WSI
SLN-Breast (Campanella et al., 2019b)	Breast	20x	H&E	130	WSI

C.1. Validation datasets

For all validation datasets, training data is comprised of 50% of total data, with 25% for both validation and testing sets, unless otherwise mentioned. For classification, we used the following five datasets: BACH challenge dataset (Aresta et al., 2019), a malignant lymphoma classification dataset which we denote as "Lymph" (Orlov et al., 2010), BreakHis (Spanhol, Oliveira, Petitjean, & Heutte, 2016), NCT-CRC-HE-100K (Kather, Halama, & Marx, 2018), and Gleason2019 (Nir et al., 2018).

The BACH challenge classification dataset contains 400 patches of size 2048 × 1536 pixels extracted from breast biopsy WSIs. The dataset

is evenly split into four classes (normal, benign, in situ carcinoma, and invasive carcinoma), and the challenge task was to automatically classify images into these classes. The Lymph dataset contains 374 H&E stained images from lymph nodes, sampled by multiple pathologists at different sites. The images are separated into three classes: CLL (chronic lymphocytic leukemia), FL (follicular lymphoma), and MCL (mantle cell lymphoma). Notably, this dataset contains a large degree of staining variation within dataset. The BreakHis dataset contains 7909 patches of size 700 × 460 pixels taken from WSIs of breast tumor tissue. The data is labeled as either benign or malignant, and images belong to one of four magnifying factors (40x, 100x, 200x, and 400x). The NCT-CRC-HE-100K dataset contains 107180 patches of size 224 × 224 pixels.

The split differs for this dataset, with 75000 patches in the training set, 25000 in validation, and 7180 in the test set. The test set comes from a related dataset called CRC-VAL-HE-7K, which was recommended for use as validation for the larger dataset. Images are taken from 86 stained colorectal cancer tissue slides. The data is split into nine classes: Adipose (ADI), background (BACK), debris (DEB), lymphocytes (LYM), mucus (MUC), smooth muscle (MUS), normal colon mucosa (NORM), cancer-associated stroma (STR), and colorectal adenocarcinoma epithelium (TUM). The Gleason2019 dataset contains 244 tissue micro-array (TMA) images from prostate biopsies. The segmentation labels for this dataset are the Gleason scores for each pixel in the image, ranging from 1 (healthy) to 5 (abnormal).

For segmentation, we used the following two datasets: BACH challenge dataset (Aresta et al., 2019), and DigestPath2019 (Li et al., 2019). The BACH segmentation dataset originates from part B of the challenge, and consists of 10 breast biopsy WSIs with pixel-level segmentation masks. These whole-slides are split 5/3/2 for train/validation/test respectively. The segmentation labels are the same 4 classes in the classification dataset. Patches of size 1024×1024 pixels were extracted from each slide with a sliding window. The DigestPath2019 challenge dataset contains $250\ 5000 \times 5000$ pixel image patches taken from colonoscopy tissue slides. For our task, we resize each patch and its corresponding pixel-level label image to 1024×1024 . The segmentation masks provided for this dataset are divided into two classes (benign or malignant), and the aim of this challenge is to use these segmentation labels to identify early-stage colon tumors.

For regression, we used the BreastPathQ dataset (Akbar, Peikari, Salama, Panah, Nofech-Mozes, & Martel, 2019). It consists of a total of 2579 patches with size 512×512 pixels extracted from 69 WSIs of Post-NAT-BRCA specimens (Peikari et al., 2017). BreastPathQ images are labeled according to the percentage of cancer cellularity in each patch. The aim is to predict the percentage cellularity given an input image patch.

Appendix D. Detailed results

See Tables D.7–D.11.

Appendix E. Comparison to other self-supervised methods

In this section, we compare SimCLR's performance to the earlier self-supervised techniques. We select each technique based on their recency. Each method uses the 1% of all available pretraining data. We repurpose the segmentation network used in our experiments (Yakubovskiy, 2020) with the Resnet50 encoder, and optimize the image reconstruction objective with L_1 loss to train an autoencoder. We use an earlier self supervised technique which is based on predicting the RGB channels of a grayscale image for learning representations (colorization) (Zhang, Isola, & Efros, 2016), and use a more recent self supervised method called CPCv2 that encodes small patches from a larger image in a sliding window. Then, the aim is to predict encoded representations based on spatial proximity (patches extracted from an image that are spatially adjacent are considered more similar) (Hénaff et al., 2019) (see Table E.12).

Appendix F. Datasets

F.1. Pretraining datasets

See Table F.13.

References

- Akbar, S., Peikari, M., Salama, S., Panah, A. Y., Nofech-Mozes, S., & Martel, A. L. (2019). Automated and manual quantification of tumour cellularity in digital slides for tumour burden assessment. *Scientific Reports*, 9(1), 14099.
- Aresta, G., Araújo, T., Kwok, S., Chennamsetty, S. S., Safwan, M., Alex, V., et al. (2019). Bach: Grand challenge on breast cancer histology images. *Medical Image Analysis*, 56, 122–139.
- Bachman, P., Hjelm, R. D., & Buchwalter, W. (2019). Learning representations by maximizing mutual information across views. In *Advances in neural information processing systems* (pp. 15509–15519).
- Becker, S., & Hinton, G. E. (1992). Self-organizing neural network that discovers surfaces in random-dot stereograms. *Nature*, 355(6356), 161–163.
- Bolhasani, H., Amjadi, E., Tabatabaeian, M., & Jassbi, S. J. (2020). A histopathological image dataset for grading breast invasive ductal carcinomas. *Informatics in Medicine Unlocked*, 19, Article 100341. <http://dx.doi.org/10.1016/j.imu.2020.100341>, URL: <https://www.sciencedirect.com/science/article/pii/S2352914820300757>.
- Campanella, G., Hanna, M., Geneslaw, L., Miraflor, A., Silva, V., Busam, K., et al. (2019a). Clinical-grade computational pathology using weakly supervised deep learning on whole slide images. *Nature Medicine*, 25, 1. <http://dx.doi.org/10.1038/s41591-019-0508-1>.
- Campanella, G., Hanna, M. G., Geneslaw, L., Miraflor, A., Werneck Krauss Silva, V., Busam, K. J., et al. (2019b). Clinical-grade computational pathology using weakly supervised deep learning on whole slide images. *Nature Medicine*, 25(8), 1301–1309. <http://dx.doi.org/10.1038/s41591-019-0508-1>.
- Capron, F., Calvo, J., Attieh, E., Naour, G. L., & Gloaguen, A. (2014). Mitos-ATYPIA-14 grand challenge. URL: <https://mitos-atypia-14.grand-challenge.org/>.
- Chang, H., Han, J., Zhong, C., Snijders, A. M., & Mao, J.-H. (2017). Unsupervised transfer learning via multi-scale convolutional sparse coding for biomedical applications. *IEEE Transactions on Pattern Analysis and Machine Intelligence*, 40(5), 1182–1194.
- Chen, T., Kornblith, S., Norouzi, M., & Hinton, G. (2020). A simple framework for contrastive learning of visual representations. arXiv preprint <arXiv:2002.05709>.
- Chen, T., Kornblith, S., Swersky, K., Norouzi, M., & Hinton, G. (2020). Big self-supervised models are strong semi-supervised learners. arXiv preprint <arXiv:2006.10029>.
- Choyke, P., Turkbey, B., Pinto, P., Merino, M., & Wood, B. (2016). Prostate-MRI dataset. <http://dx.doi.org/10.7937/K9/TCIA.2016.6046GUDv>.
- Ciga, O., Xu, T., Nofech-Mozes, S., Noy, S., Lu, F.-I., & Martel, A. L. (2021). Overcoming the limitations of patch-based learning to detect cancer in whole slide images. *Scientific Reports*, 11(1), 1–10.
- Dosovitskiy, A., Springenberg, J. T., Riedmiller, M., & Brox, T. (2014). Discriminative unsupervised feature learning with convolutional neural networks. In *Advances in neural information processing systems* (pp. 766–774).
- Ehteshami Bejnordi, B., Veta, M., Johannes van Diest, P., van Ginneken, B., Karssemeijer, N., Litjens, G., et al. (2017). Diagnostic assessment of deep learning algorithms for detection of lymph node metastases in women with breast cancer. *JAMA*, 318(22), 2199–2210. <http://dx.doi.org/10.1001/jama.2017.14585>.
- Gamper, J., Koohbanani, N. A., Benet, K., Khuram, A., & Rajpoot, N. (2019). Pan-Nuke: an open pan-cancer histology dataset for nuclei instance segmentation and classification. In *European congress on digital pathology* (pp. 11–19). Springer.
- Gehlot, S., Gupta, A., & Gupta, R. (2019). All challenge dataset of ISBI 2019. <http://dx.doi.org/10.7937/tcia.2019.dc64i46r>.
- Gidaris, S., Singh, P., & Komodakis, N. (2018). Unsupervised representation learning by predicting image rotations. arXiv preprint <arXiv:1803.07728>.
- Gildenblat, J., & Klaiman, E. (2019). Self-supervised similarity learning for digital pathology. arXiv preprint <arXiv:1905.08139>.
- Graham, S., Vu, Q. D., Raza, S. E. A., Azam, A., Tsang, Y. W., Kwak, J. T., et al. (2019). Hover-net: Simultaneous segmentation and classification of nuclei in multi-tissue histology images. *Medical Image Analysis*, 58, Article 101563. <http://dx.doi.org/10.1016/j.media.2019.101563>, URL: <https://www.sciencedirect.com/science/article/pii/S1361841519301045>.
- Grill, J.-B., Strub, F., Altché, F., Tallec, C., Richemond, P. H., Buchatskaya, E., et al. (2020). Bootstrap your own latent: A new approach to self-supervised learning. arXiv preprint <arXiv:2006.07733>.
- Gupta, A. (2018). MiMM_SBiLab Dataset: Microscopic images of multiple myeloma. <http://dx.doi.org/10.7910/DVN/XCX7ST>.
- Gupta, A., & Gupta, R. (2019). SN-AM Dataset: White blood cancer dataset of B-ALL and MM for stain normalization. <http://dx.doi.org/10.7937/tcia.2019.of2w8lxr>.
- He, K., Fan, H., Wu, Y., Xie, S., & Girshick, R. (2020). Momentum contrast for unsupervised visual representation learning. In *Proceedings of the IEEE/CVF conference on computer vision and pattern recognition* (pp. 9729–9738).
- He, K., Zhang, X., Ren, S., & Sun, J. (2016). Deep residual learning for image recognition. In *2016 IEEE conference on computer vision and pattern recognition* (pp. 770–778). <http://dx.doi.org/10.1109/CVPR.2016.90>.
- Hénaff, O. J., Srinivas, A., De Fauw, J., Razavi, A., Doersch, C., Eslami, S., et al. (2019). Data-efficient image recognition with contrastive predictive coding. arXiv preprint <arXiv:1905.09272>.
- Hou, L., Nguyen, V., Kanevsky, A. B., Samaras, D., Kurc, T. M., Zhao, T., et al. (2019). Sparse autoencoder for unsupervised nucleus detection and representation in histopathology images. *Pattern Recognition*, 86, 188–200.

- Hu, B., Tang, Y., Eric, I., Chang, C., Fan, Y., Lai, M., et al. (2018). Unsupervised learning for cell-level visual representation in histopathology images with generative adversarial networks. *IEEE Journal of Biomedical and Health Informatics*, 23(3), 1316–1328.
- Jack, N. P., Thomas, W., Marick, L., & Fabien, R. (2018). Segmentation of nuclei in histopathology images by deep regression of the distance map. <http://dx.doi.org/10.5281/zenodo.1175282>, We would like to thank Ligue National contre le Cancer for funding my PhD.
- Janowczyk, A., & Madabhushi, A. (2016). Deep learning for digital pathology image analysis: A comprehensive tutorial with selected use cases. *Journal of Pathology Informatics*, 7(1), 29. <http://dx.doi.org/10.4103/2153-3539.186902>, URL: <https://www.jpathinformatics.org/article.asp?issn=2153-3539;year=2016;volume=7;issue=1;spage=29;epage=29;aulast=Janowczyk;t=6>.
- Kather, J. N., Halama, N., & Marx, A. (2018). 100,000 histological images of human colorectal cancer and healthy tissue. <http://dx.doi.org/10.5281/zenodo.1214456>.
- Kingma, D. P., & Ba, J. (2014). Adam: A method for stochastic optimization. arXiv preprint [arXiv:1412.6980](https://arxiv.org/abs/1412.6980).
- Komura, D., & Ishikawa, S. (2018). Machine learning methods for histopathological image analysis. *Computational and Structural Biotechnology Journal*, 16, 34–42.
- Kumar, N., Verma, R., Anand, D., Zhou, Y., Onder, O. F., Tsougenis, E., et al. (2020). A multi-organ nucleus segmentation challenge. *IEEE Transactions on Medical Imaging*, 39(5), 1380–1391. <http://dx.doi.org/10.1109/TMI.2019.2947628>.
- Kuse, M., Wang, Y.-F., Kalasanavar, V., Khan, M., & Rajpoot, N. (2011). Local isotropic phase symmetry measure for detection of beta cells and lymphocytes. *Journal of Pathology Informatics*, 2, S2. <http://dx.doi.org/10.4103/2153-3539.92028>.
- Li, J., Yang, S., Huang, X., Da, Q., Yang, X., Hu, Z., et al. (2019). Signet ring cell detection with a semi-supervised learning framework. In *International conference on information processing in medical imaging* (pp. 842–854). Springer.
- Litjens, G., Bandi, P., Ehteshami Bejnordi, B., Geessink, O., Balkenhol, M., Bult, P., et al. (2018). 1399 h&e-stained sentinel lymph node sections of breast cancer patients: the CAMELYON dataset. *GigaScience*, 7(6), giy065.
- Martel, A. L., Nofech-Mozes, S., Salama, S., Akbar, S., & Peikari, M. (2019). Assessment of residual breast cancer cellularity after neoadjuvant chemotherapy using digital pathology. <https://doi.org/10.7937/TCIA.2019.4YIBTJNO> [Data set].
- Matek, C., Schwarz, S., Spiekermann, K., & Marr, C. (2019). A single-cell morphological dataset of leukocytes from AML patients and non-malignant controls. <http://dx.doi.org/10.7937/tcia.2019.36f5o9ld>.
- Mehra, R., et al. (2018). Breast cancer histology images classification: Training from scratch or transfer learning? *ICT Express*, 4(4), 247–254.
- Mikolov, T., Chen, K., Corrado, G., & Dean, J. (2013). Efficient estimation of word representations in vector space. arXiv preprint [arXiv:1301.3781](https://arxiv.org/abs/1301.3781).
- Misra, I., & Maaten, L. v. d. (2020). Self-supervised learning of pretext-invariant representations. In *Proceedings of the IEEE/CVF conference on computer vision and pattern recognition* (pp. 6707–6717).
- Nir, G., Hor, S., Karimi, D., Fazli, L., Skinnider, B. F., Tavassoli, P., et al. (2018). Automatic grading of prostate cancer in digitized histopathology images: Learning from multiple experts. *Medical Image Analysis*, 50, 167–180. <http://dx.doi.org/10.1016/j.media.2018.09.005>, URL: <http://www.sciencedirect.com/science/article/pii/S1361841518307497>.
- Noroozi, M., & Favaro, P. (2016). Unsupervised learning of visual representations by solving jigsaw puzzles. In *European conference on computer vision* (pp. 69–84).
- Orlov, N., Chen, W., Eckley, D., Macura, T., Shamir, L., Jaffe, E., et al. (2010). Automatic classification of lymphoma images with transform-based global features. *IEEE Transactions on Information Technology in Biomedicine : A Publication of the IEEE Engineering in Medicine and Biology Society*, 14, 1003–1013. <http://dx.doi.org/10.1109/TITB.2010.2050695>.
- Peikari, M., Salama, S., Nofech-Mozes, S., & Martel, A. L. (2017). Automatic cellularity assessment from post-treated breast surgical specimens. *Cytometry Part A*, 91(11), 1078–1087.
- Peikari, M., Salama, S., Nofech-Mozes, S., & Martel, A. L. (2018). A cluster-thenn-label semi-supervised learning approach for pathology image classification. *Scientific Reports*, 8(1), 1–13.
- Raza, S. e. A., Humayun, A., Abouna, S., Nattkemper, T., Epstein, D., Khan, M., et al. (2012). Ramtab: Robust alignment of multi-tag bioimages. *PLoS One*, 7, Article e30894. <http://dx.doi.org/10.1371/journal.pone.0030894>.
- Ronneberger, O., Fischer, P., & Brox, T. (2015). U-net: Convolutional networks for biomedical image segmentation. In *International conference on medical image computing and computer-assisted intervention* (pp. 234–241). Springer.
- Roux, L., Racoceanu, D., Lomenie, N., Kulikova, M., Irshad, H., Klossa, J., et al. (2013). Mitosis detection in breast cancer histological images an ICPR 2012 contest. *Journal of Pathology Informatics*, 4, 8. <http://dx.doi.org/10.4103/2153-3539.112693>.
- Russakovsky, O., Deng, J., Su, H., Krause, J., Satheesh, S., Ma, S., et al. (2015). ImageNet Large scale visual recognition challenge. *International Journal of Computer Vision (IJCV)*, 115(3), 211–252. <http://dx.doi.org/10.1007/s11263-015-0816-y>.
- Schroff, F., Kalenichenko, D., & Philbin, J. (2015). Facenet: A unified embedding for face recognition and clustering. In *Proceedings of the IEEE conference on computer vision and pattern recognition* (pp. 815–823).
- Sirinukunwattana, K., Pluim, J. P. W., Chen, H., Qi, X., Heng, P.-A., Guo, Y. B., et al. (2016). Gland segmentation in colon histology images: The glas challenge contest. [arXiv:1603.00275](https://arxiv.org/abs/1603.00275).
- Sirinukunwattana, K., Raza, S. E. A., Tsang, Y., Snead, D. R. J., Cree, I. A., & Rajpoot, N. M. (2016). Locality sensitive deep learning for detection and classification of nuclei in routine colon cancer histology images. *IEEE Transactions on Medical Imaging*, 35(5), 1196–1206. <http://dx.doi.org/10.1109/TMI.2016.2525803>.
- Spanhol, F. A., Oliveira, L. S., Petitjean, C., & Heutte, L. (2016). A dataset for breast cancer histopathological image classification. *IEEE Transactions on Biomedical Engineering*, 63(7), 1455–1462.
- Swiderska-Chadaj, Z., Pinckaers, H., van Rijthoven, M., Balkenhol, M., Melnikova, M., Geessink, O., et al. (2019). Learning to detect lymphocytes in immunohistochemistry with deep learning. *Medical Image Analysis*, 58, Article 101547. <http://dx.doi.org/10.1016/j.media.2019.101547>, URL: <https://www.sciencedirect.com/science/article/pii/S1361841519300829>.
- Tajbakhsh, N., Shin, J. Y., Gurudu, S. R., Hurst, R. T., Kendall, C. B., Gotway, M. B., et al. (2016). Convolutional neural networks for medical image analysis: Full training or fine tuning? *IEEE Transactions on Medical Imaging*, 35(5), 1299–1312.
- Tarvainen, A., & Valpola, H. (2017). Mean teachers are better role models: Weight-averaged consistency targets improve semi-supervised deep learning results. In *Advances in neural information processing systems* (pp. 1195–1204).
- Tellez, D., Litjens, G., van der Laak, J., & Ciompi, F. (2019). Neural image compression for gigapixel histopathology image analysis. *IEEE Transactions on Pattern Analysis and Machine Intelligence*.
- Tian, Y., Krishnan, D., & Isola, P. (2019). Contrastive multiview coding. arXiv preprint [arXiv:1906.05849](https://arxiv.org/abs/1906.05849).
- Veta, M., Heng, Y. J., Stathonikos, N., Bejnordi, B. E., Beca, F., Wollmann, T., et al. (2019). Predicting breast tumor proliferation from whole-slide images: The TUPAC16 challenge. *Medical Image Analysis*, 54, 111–121. <http://dx.doi.org/10.1016/j.media.2019.02.012>.
- Wu, Z., Xiong, Y., Yu, S., & Lin, D. (2018). Unsupervised feature learning via non-parametric instance-level discrimination. arXiv preprint [arXiv:1805.01978](https://arxiv.org/abs/1805.01978).
- Xu, J., Xiang, L., Liu, Q., Gilmore, H., Wu, J., Tang, J., et al. (2015). Stacked sparse autoencoder (SSAE) for nuclei detection on breast cancer histopathology images. *IEEE Transactions on Medical Imaging*, 35(1), 119–130.
- Yakubovskiy, P. (2020). Segmentation models pytorch.
- You, Y., Gitman, I., & Ginsburg, B. (2017). Large batch training of convolutional networks. *Computer Vision and Pattern Recognition, ArXiv*.
- You, Y., Li, J., Reddi, S., Hsieu, J., Kumar, S., Bhojanapalli, S., et al. (2019). Large batch optimization for deep learning: Training bert in 76 minutes. In *International conference on learning representations* (p. 1).
- Zhang, R., Isola, P., & Efros, A. A. (2016). Colorful image colorization. In *European conference on computer vision* (pp. 649–666). Springer.